Optimal spin-charge interconversion in graphene through spin-pseudospin entanglement control

Joaquín Medina Dueñas,[1,2,*] Santiago Giménez de Castro,[1] José H. García,[1,†] and Stephan Roche[1,3]

[1] *Institut Català de Nanociència i Nanotecnologia (ICN2), CSIC and BIST, Campus UAB, Bellaterra 08193, Barcelona, Spain*
[2] *Department of Physics, Universitat Autònoma de Barcelona (UAB), Campus UAB, Bellaterra, 08193 Barcelona, Spain*
[3] *ICREA — Institució Catalana de Recerca i Estudis Avançats, 08010 Barcelona, Spain*

(Dated: April 14, 2026)

The electrical generation of spin signals is of central interest for spintronics, where graphene stands as a relevant platform as its spin-orbit coupling (SOC) is tuned by proximity effects. Here, we propose an enhancement of spin-charge interconversion in graphene by controlling the intra-particle entanglement between the spin and pseudospin degrees of freedom. We demonstrate that, although the spin alone is not conserved in Rashba-Dirac systems, a combined spin-pseudospin operator is conserved. This conserved quantity represents the interconversion between pure spin and pseudospin textures to a spin-pseudospin entangled structure, where Kane-Mele SOC tunes this balance. By these means, we achieve spin-charge interconversion of 100% efficiency via the Rashba-Edelstein effect. Quantum transport simulations in disordered micron-size systems demonstrate the robustness of this effect, and also reveal a disorder resilient spin Hall effect generated by the interplay between Rashba and Kane-Mele SOC. Our findings propose a platform for maximally efficient spin-charge interconversion, and establish spin-pseudospin correlations as a mechanism to tailor spintronic devices.

INTRODUCTION

Spin-charge interconversion (SCI) mechanisms lie at the core of spintronic technologies, generating current-driven spin signals which can then be used for information processing [1, 2]. Traditionally, the development of efficient SCI relies on bulk heavy metals with a large spin-orbit coupling (SOC); however, van der Waals materials offer new possibilities as SOC can be tuned by proximity effects [3–5]. Graphene is particularly relevant in this context [6, 7]. Its long spin diffusion length makes it an ideal platform for spin transport and spin logic operations [8–11]; while SOC can be induced and tailored by proximity effects stacking graphene with transition metal dichalcogenides (TMDs) [12–18] or topological insulators (TIs) [19–22]. Efficient SCI via the Rashba-Edelstein effect (REE, also called inverse spin galvanic effect) and the spin Hall effect (SHE) has been shown in graphene-based heterostructures [23–26], even outperforming bulk heavy metals and non-van der Waals interfaces [25]; with the additional advantage of gate-tunability.

Most of graphene's unique features emerge from pseudospin related effects [27–31], where the pseudospin degree of freedom stemming from its bipartite sublattice structure generates the characteristic massless Dirac fermion behaviour. SOC in graphene is mediated by the pseudospin, and thus spin-pseudospin correlations play a central role in spin-related transport. Indeed, the weak localisation to weak antilocalisation transition in graphene is driven by both pseudospin and spin coherence effects [32, 33]; while the spin relaxation near the Dirac point is dominated by intra-particle spin-pseudospin entanglement [34], as well as the electric dipole spin resonance [35]. However, the role of spin-pseudospin correlations in SCI has not been fully understood. While graphene exhibits a unique vertical Rashba splitting enabling an efficient REE [36, 37], spin-pseudospin entanglement is most prominent in this regime [37, 38]. More recently, spin-pseudospin entanglement was proposed to drive spin-orbit torques in graphene beyond the electron gas regime generating unconventional spin-orbit torque fields [39, 40].

Here, we propose an enhanced SCI regime in graphene by controlling spin-pseudospin entanglement. We demonstrate the manipulation of spin-pseudospin entanglement by tuning different SOC fields; namely, Rashba and Kane-Mele (also called intrinsic) SOC. While spin angular momentum is not a conserved quantity due to Rashba SOC, we show that a combined spin-pseudospin operator is conserved, representing the interconversion between pure spin and pseudospin textures to a spin-pseudospin entangled structure, where Kane-Mele SOC tunes the spin-entanglement balance. By these means, the REE is optimised up to maximal efficiency of 100%, surpassing the previous theoretical maximum predicted in structures without Kane-Mele SOC [37]. We furthermore demonstrate the enhanced REE is highly robust by performing real-space simulations of micron-scale systems including disorder, maintaining a nearly maximal efficiency. Additionally, we demonstrate that Kane-Mele SOC reinstates a finite SHE in Rashba-Dirac systems even in presence of disorder, which is otherwise suppressed [41].

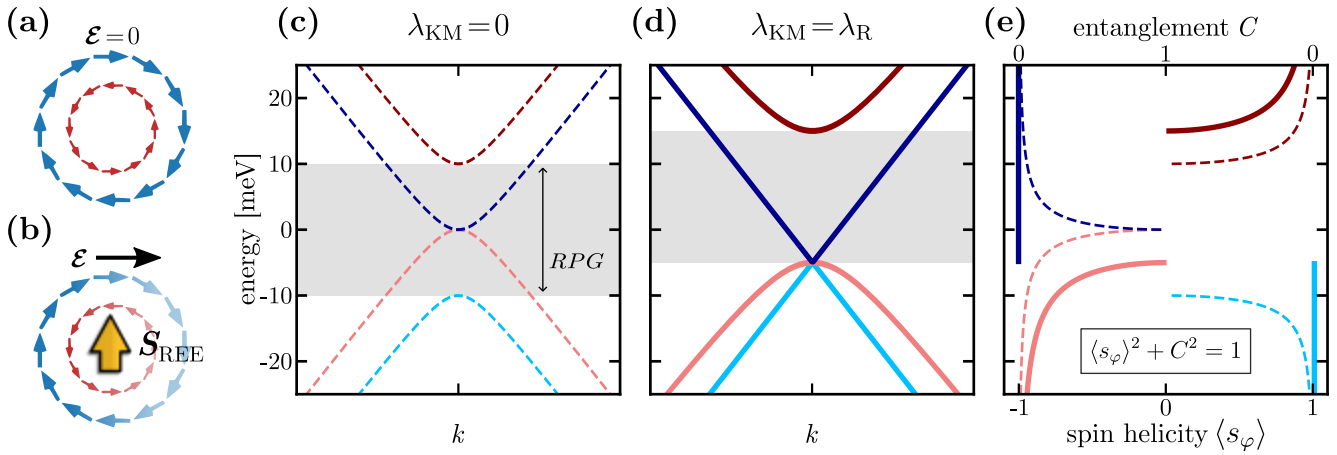

FIG. 1. Depiction of the Rashba-Edelstein effect (REE) originating from helical spin textures in graphene. (a) Depiction of the Fermi contours with helical spin-momentum locking, represented by the blue and red arrows, with no applied electric field ($\boldsymbol{\mathcal{E}}=0$). (b) Depiction of the REE, where the applied electric field $\boldsymbol{\mathcal{E}}$ generates a carrier redistribution, represented by the faded Fermi contours, generating a net spin density $\boldsymbol{S}_{\mathrm{REE}}\propto\hat{\boldsymbol{z}}\times\boldsymbol{\mathcal{E}}$ (yellow arrow) (c, d) Band structure for (c) $\lambda_{\mathrm{KM}}=0$ and (d) $\lambda_{\mathrm{KM}}=\lambda_{\mathrm{R}}=10\,\mathrm{meV}$, with λ_{KM} and λ_{R} the Kane-Mele and Rashba spin-orbit coupling (SOC) parameters. The Rashba pseudogap (RPG) is shaded in gray, while the light and dark red (blue) curves correspond to the $\chi=+$ ($\chi=-$) subspace, as defined in Eq. (2). (e) Spin helicity (bottom axis) and spin-pseudospin entanglement (top axis) of the bands. Kane-Mele SOC reduces the effective mass in the blue cone, suppressing entanglement and enhancing the spin helicity throughout the pseudogap, leading to a larger REE.

RESULTS AND DISCUSSION

In the REE, broken mirror symmetry parallel to the two-dimensional plane induces helical spin-momentum locking via Rashba SOC, where the spin texture winds about the Fermi contour orthogonal to the momentum. When applying a current, the non-equilibrium carrier redistribution generates a net spin density of the form $\boldsymbol{S}_{\mathrm{REE}}\propto\hat{\boldsymbol{z}}\times\boldsymbol{\mathcal{E}}$, with $\boldsymbol{\mathcal{E}}$ the driving electric field, as depicted in panels (a) and (b) of Fig. 1. Vertical Rashba splitting in graphene generates favourable conditions for the REE as the current is carried through a single spin-helical band near the charge neutrality point [37]. However, because the pseudospin mediates spin-momentum locking, the spin texture is quenched by spin-pseudospin entanglement, representing the main limiting factor for the REE efficiency. Controlling spin-pseudospin entanglement thus emerges as the path towards optimizing SCI, as demonstrated in the following.

We consider a minimal graphene model endowed with Rashba SOC and Kane-Mele SOC. The low-energy Bloch Hamiltonian is

$$\mathcal{H}_{\boldsymbol{k}}=\hbar v_{\mathrm{gr}}\left(k_x\tau_z\sigma_x+k_y\sigma_y\right)-\frac{\lambda_{\mathrm{R}}}{2}\left(\sigma_y s_x-\tau_z\sigma_x s_y\right)-\frac{\lambda_{\mathrm{KM}}}{2}\tau_z\sigma_z s_z\ , \tag{1}$$

with $v_{\mathrm{gr}}\sim 10^6\,\mathrm{m\,s^{-1}}$ the velocity of massless electrons in bare graphene, and λ_{R} and λ_{KM} the Rashba and Kane-Mele SOC parameters respectively. The spin, pseudospin and valley degrees of freedom are respectively represented by the Pauli vectors $\boldsymbol{s}$, $\boldsymbol{\sigma}$ and $\boldsymbol{\tau}$. We will focus our analysis on the $\tau_z=+1$ subspace without loss of generality, as shown in the Supplementary Note S1. Kane-Mele SOC has been shown to be enhanced up to the meV scale in graphene/TI heterostructures [19, 21], while the emergence of Rashba SOC depends on the stacking and is typically smaller [20–22]. On the other hand, in graphene/TMD bilayers Rashba SOC can range up to $\sim 15\,\mathrm{meV}$ [13, 14, 42], while Kane-Mele SOC is negligible, but could be enhanced by decoration with adatoms [43, 44] or nanoparticles [45].

At large momentum the bare graphene Hamiltonian dominates, represented by the first term in Eq. (1); and thus the bands are completely pseudospin polarised along the radial direction, $\langle\boldsymbol{\sigma}\rangle=\pm\hat{\boldsymbol{k}}$. Each subset of bands splits into clockwise and counter-clockwise spin helicity due to Rashba SOC, $\langle\boldsymbol{s}\rangle=\pm\hat{\boldsymbol{\varphi}}=\pm\hat{\boldsymbol{z}}\times\hat{\boldsymbol{k}}$, while Kane-Mele SOC does not influence the band structure in this regime. The resulting eigenstates, labelled by the radial pseudospin direction μ and spin helicity ξ (with $\mu,\xi=\pm$), have the fully disentangled form $|\mu,\xi\rangle=|\mu\hat{\boldsymbol{k}}\rangle_\sigma\otimes|\xi\hat{\boldsymbol{\varphi}}\rangle_s$, where the first and second components correspond to the pseudospin and spin projected substates, which are the respective eigenstates of the operators $\sigma_k=\boldsymbol{\sigma}\cdot\hat{\boldsymbol{k}}$ and $s_\varphi=\boldsymbol{s}\cdot\hat{\boldsymbol{\varphi}}$. Near the Dirac point, however, the SOC terms become of comparable strength to the bare graphene hamiltonian, resulting in the hybridisation of the asymptotic pure states and emergence of spin-pseudospin entanglement.

We express the Hamiltonian in the asymptotic eigenbasis, revealing that the spectrum separates in two decou-

pled Dirac cones, one for each spin-pseudospin winding direction, labelled by $\chi = \text{sign}\,\langle \boldsymbol{\sigma} \times \boldsymbol{s} \rangle \cdot \hat{\boldsymbol{z}}$. The Hamiltonian projected to subspace χ reads

$$\mathcal{H}_{\boldsymbol{k},\chi} = \chi \frac{\lambda_{\rm R}}{2} \mathbb{1}_{2\times 2} - \begin{pmatrix} +\hbar v_{\rm gr} k & \frac{1}{2}(\lambda_{\rm KM} + \chi\lambda_{\rm R}) \\ \frac{1}{2}(\lambda_{\rm KM} + \chi\lambda_{\rm R}) & -\hbar v_{\rm gr} k \end{pmatrix} , \tag{2}$$

where the matrix elements correspond to the basis of pure states $|-,-\chi\rangle$ and $|+,+\chi\rangle$. The cones are gapped by an effective mass of magnitude $|\Delta_\chi| = |\lambda_{\rm R} + \chi\lambda_{\rm KM}|$, which promotes maximally entangled states of the form $\frac{1}{\sqrt{2}}(|-,-\chi\rangle \pm |+,+\chi\rangle)$ at $k = 0$. The resulting bands are $E_{\chi,\pm} = \chi\lambda_{\rm R}/2 \pm \varepsilon_\chi$, with $\varepsilon_\chi = [(\hbar v_{\rm gr} k)^2 + \Delta_\chi^2/4]^{1/2}$, while the spin and pseudospin textures are $\langle \boldsymbol{s} \rangle_{\chi,\pm} = \pm\chi\rho_\chi \hat{\boldsymbol{\varphi}}$ and $\langle \boldsymbol{\sigma} \rangle_{\chi,\pm} = \pm\rho_\chi \hat{\boldsymbol{k}}$, with $\rho_\chi = \hbar v_{\rm gr} k/\varepsilon_\chi$, where we have dropped the $\boldsymbol{k}$ index for simplicity (see Supplementary Note S1 for complete calculations). We note that Kane-Mele SOC, unlike other interactions such as a valley-Zeeman SOC, preserves the nature of the Rashba-Dirac system, marked by the spin-pseudospin winding of the bands.

The spin and pseudospin textures respectively remain fully helical and radial, but their magnitudes are quenched near the Dirac point. Because of SOC, the pure spin and pseudospin angular momenta are not conserved quantities, but these rather take the form of coupled spin-pseudospin operators. In particular we obtain the conserved quantity $\mathcal{Q} = \sigma_k s_\varphi$, with eigenvalues $\langle \mathcal{Q} \rangle_{\chi,\pm} = \chi$. The separable contribution to $\langle \mathcal{Q} \rangle$ is given by $\langle \mathcal{Q} \rangle_{\rm sep} = \langle \sigma_k \rangle \langle s_\varphi \rangle$, and is determined by the pure spin and pseudospin textures. On the other hand, we find that the non-separable contribution, given by $\langle \mathcal{Q} \rangle - \langle \mathcal{Q} \rangle_{\rm sep}$, is determined by the spin-pseudospin entanglement, as $\langle \sigma_k s_\varphi \rangle_{\chi,\pm} - \langle \sigma_k \rangle_{\chi,\pm} \langle s_\varphi \rangle_{\chi,\pm} = \chi C^2_{\chi,\pm}$, where C is the concurrence, which quantifies entanglement from 0 to 1 from pure to maximally entangled states respectively [38, 46] (see Supplementary Note S1 for explicit calculation). We conclude that the conserved quantity $\mathcal{Q} = \sigma_k s_\varphi$ represents the interconversion of angular momentum from the individual spin and pseudospin projections to spin-pseudospin entanglement. Finally, by expressing this relation as

$$\langle \boldsymbol{s} \rangle^2_{\chi,\pm} + C^2_{\chi,\pm} = 1 , \tag{3a}$$

$$\langle \boldsymbol{\sigma} \rangle^2_{\chi,\pm} + C^2_{\chi,\pm} = 1 , \tag{3b}$$

we explicitly show that the entanglement is proportional to the quenching of the individual spin and pseudospin textures.

The spin texture throughout the Rashba pseudogap is enhanced by including Kane-Mele SOC, as shown in panels (c) and (d) of Fig. 1, for $\lambda_{\rm KM} = 0$ and $\lambda_{\rm KM} = \lambda_{\rm R}$, respectively, while the light and dark red (blue) curves correspond to the $\chi = +$ ($\chi = -$) cone. The energy gap of the red $\chi = +$ (blue $\chi = -$) cone is crossed by the

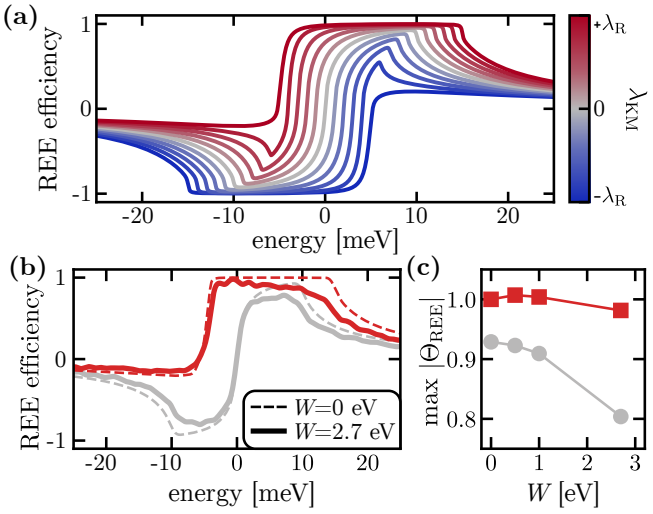

FIG. 2. REE results. Panels (a) and (b) show the Rahbsa-Edelstein effect (REE) efficiency, $\Theta_{\rm REE}$, as a function of the Fermi energy in the constant broadening approximation and in the real-space disordered system, respectively. The REE is optimised up to maximal efficiency $\Theta_{\rm REE} = \pm 1$ for Kane-Mele and Rashba spin-orbit coupling parameters of equal magnitude ($\lambda_{\rm KM} = \pm\lambda_{\rm R}$) in the constant broadening approximation , remaining robust against disorder. Panel (c) shows the maximum $|\Theta_{\rm REE}|$ as a function of the disorder strength W. In all panels, the colour of the curves indicates the value of $\lambda_{\rm KM}$ according to the colourbar. [$\lambda_{\rm R} = 10\,$meV]

upper (lower) band of the opposite cone, forming the Rashba pseudogap, shaded in gray, where the Fermi level is intersected by a single spin helical band. Kane-Mele SOC opens the gap of the red $\chi = +$ cone, while that of the blue $\chi = -$ cone closes, reducing spin-pseudospin entanglement in the latter and enhancing the spin helicity throughout the pseudogap, as shown in panel (d). By these means, the spin texture can be tuned in the low-energy regime allowing to optimise the REE up to maximal efficiency, which we demonstrate below.

We quantify the REE efficiency adopting the definition proposed by Offidani, et al.[37], which corresponds to the ratio between the transversal non-equilibrium spin density S_y, and the charge current J_x, yielding the efficiency $\Theta_{\rm REE} = 2ev S_y/(\hbar J_x)$. Here v corresponds to the transport velocity required to adimensionalise the spin-to-current ratio. Within a perturbative treatment of disorder, v remounts to the Fermi velocity obtained from the band structure, $v_{\rm F} = \hbar^{-1}\partial E/\partial k$, as originally considered[37]. We extend this definition beyond the perturbative regime in order to further explore the robustness of SCI, as discussed in the Methods section.

We compute the non-equilibrium spin density at Fermi level $\varepsilon_{\rm F}$ using the Kubo-Bastin formula [47], yielding

$$S_y(\varepsilon_{\rm F}) = \frac{\hbar\mathcal{E}}{\pi\Omega} \int {\rm d}\varepsilon\, f(\varepsilon) {\rm Im\,Tr}\Big[{\rm Im} G^+ \frac{\hbar}{2} s_y \frac{\partial G^+}{\partial \varepsilon} j_x \Big] , \tag{4}$$

with f the Fermi-Dirac distribution (we take the zero temperature limit), $G^+ = \lim_{\eta\to 0^+}[\varepsilon - H + \mathrm{i}\eta]^{-1}$ the retarded Green's function, Ω the system size, $\mathcal{E}$ the driving electric field (taken along the x axis), and H and $\boldsymbol{j}$ the Hamiltonian and current operators respectively. The longitudinal current is computed identically, but replacing the spin operator $\frac{\hbar}{2}s_y$ by the current operator j_x. We refer the reader to the methods section for further detail.

We first consider a simplified transport framework, where the only effect of disorder is to introduce a constant energy broadening $\eta > 0$ in the Green's function while the Hamiltonian is perfectly pristine. We refer to this framework as the *constant broadening* approximation. For η smaller than all other energy scales, the finite broadening translates into a finite relaxation time $\tau_\eta = \hbar/2\eta$. This approach is equivalent to the semiclassical Boltzmann transport regime within the constant relaxation time approximation, and only captures the effects of a finite lifetime of the non-equilibrium quasiparticles, while omitting higher order scattering processes such as skew scattering or side-jump scattering [1]. We obtain for the non-equilibrium expectation values

$$S_y(\varepsilon_\mathrm{F}) = -\frac{e\mathcal{E}\tau_\eta}{4\pi\hbar}\sum_{k_\mathrm{F}} k\,\frac{\hbar}{2}\langle s_\varphi\rangle\,\mathrm{sign}\,\langle\sigma_k\rangle\ , \tag{5a}$$

$$J_x(\varepsilon_\mathrm{F}) = \frac{e^2 v_\mathrm{gr}\mathcal{E}\tau_\eta}{4\pi\hbar}\sum_{k_\mathrm{F}} k\,|\langle\sigma_k\rangle|\ , \tag{5b}$$

where the sum is performed over all Fermi momenta. Both S_y and J_x are Fermi surface phenomena, proportional to τ_η, and therefore the REE efficiency is independent of the chosen broadening. Within the pseudogap there is a single Fermi momenta and Θ_REE is uniquely determined by the spin helicity of the gap-crossing band, i.e. $\Theta_\mathrm{REE} = \langle s_\varphi\rangle\,\mathrm{sign}\langle\sigma_k\rangle|_{k_\mathrm{F}}$; while outside the pseudogap bands of opposite helicities counteract. Thus, the REE is maximised at the pseudogap edges, yielding

$$\max\Theta_\mathrm{REE} = \frac{2\sqrt{2\lambda_\mathrm{R}(\lambda_\mathrm{R}+\lambda_\mathrm{KM})}}{3\lambda_\mathrm{R}+\lambda_\mathrm{KM}}\ , \tag{6}$$

where we have considered $\lambda_\mathrm{R}, \lambda_\mathrm{KM} \geq 0$. $\Theta_\mathrm{REE}(\varepsilon_\mathrm{F})$ is shown in Fig. 2-(a) for different values of λ_KM, demonstrating the enhancement of the REE due to Kane-Mele SOC. Not only does the maximum value of $|\Theta_\mathrm{REE}|$ increase with λ_KM, but it also peaks throughout a wider spectral range. Remarkably, the REE is optimised up to maximal efficiency of $\Theta_\mathrm{REE} = \pm 1$ for $\lambda_\mathrm{KM} = \pm\lambda_\mathrm{R}$ due to the complete suppression of spin-pseudospin entanglement throughout the Rashba pseudogap, surpassing the previous theoretical maximum [37].

Beyond the constant broadening approximation, we demonstrate the robustness of the enhanced REE by performing real-space simulations in disordered systems, treating impurity scattering in a non-perturbative fashion. Because we intend to discern transport phenomena within the Rashba pseudogap, we require a spectral resolution on the meV scale, where a large system size is necessary to avoid spurious finite-size effects. For this, we compute Eq. (4) by the Kernel Polynomial method, developing an energy-filtering technique [48–51], which allows us to simulate a graphene sheet of $\sim 28\,\mu\mathrm{m}^2$ ($\sim 10^9$ atoms) with a numerical Jackson spectral broadening of $\eta \sim 1\,\mathrm{meV}$ generated by the finite polynomial expansion. Anderson disorder is included as random on-site potentials in the range $[-W/2, W/2]$, and is treated on equal footing to the pristine Hamiltonian. The relaxation time is now determined by both the methodology-induced quasiparticle lifetime τ_η, as well as by scattering with the disorder potential, represented by τ_p, yielding the total relaxation time $\tau^{-1} = \tau_\eta^{-1} + \tau_p^{-1}$ [49]. Furthermore, the non-perturbative treatment of disorder considers scattering effects beyond the semiclassical constant relaxation time approximation. We refer the reader to the Methods section for further detail on the methodology.

Our results reveal a remarkable robustness of the REE, with the REE efficiency shown in Fig. 2-(b, c), while the raw S_y and J_x calculations are presented in Supplementary Note S3. Indeed, both S_y and J_x scale with the relaxation time as they are Fermi surface phenomena, and are therefore suppressed with stronger disorder, where the disorder-induced suppression is weaker within the RPG, granted by a larger τ_p. The REE efficiency, on the other hand, characterises the ratio of electric current converted to spin density, and is more robust to the effects of disorder, as shown in Fig. 2-(b). The largest efficiency losses occur at the pseudogap edges, where disorder-induced scattering enables transitions between bands of opposite helicities, thus breaking the RPG regime. For $\lambda_\mathrm{KM} = 0$ we observe that the Θ_REE peak, which in the constant broadening approximation occurs at the RPG edges, is reduced by the disorder-induced smearing of the RPG, as shown in Fig. 2-(b). On the other hand, for $\lambda_\mathrm{KM} = \lambda_\mathrm{R}$, the plateau-shaped maximum grants further robustness to the REE, with the $|\Theta_\mathrm{REE}|$ peak value nearly fully preserved for all disorder intensities explored.

We now show that SCI via the SHE is also enhanced by modifying spin-pseudospin entanglement. While in the Kane-Mele dominated system the SHE is topological and robust to disorder [52, 53], in a pure Rashba-Dirac system the intrinsic contribution to the SHE is countered by disorder [41, 54]. Therefore, we focus on the $\lambda_\mathrm{KM} < \lambda_\mathrm{R}$ regime. Theoretical calculations of the intrinsic contribution have shown the emergence of a peak in the SHE within the RPG due to Kane-Mele SOC [55]; however, its response against disorder remains unexplored. To address this issue we compute the spin Hall current in real-space disordered systems using Eq. (4), replacing $\hbar s_y/2$

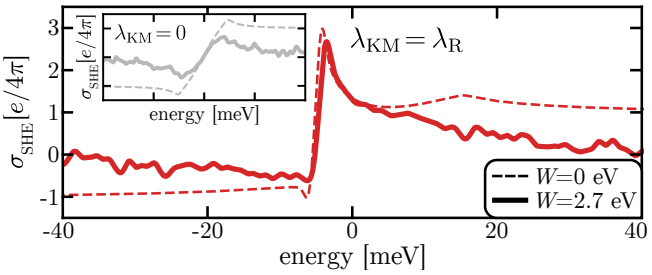

FIG. 3. Spin Hall effect (SHE) conductivity, $\sigma_{\rm SHE}$, for $\lambda_{\rm KM} = \lambda_{\rm R}$ (main panel) and $\lambda_{\rm KM} = 0$ (inset), without disorder and with disorder of $W = 2.7\,$eV, respectively shown in dashed and solid lines. $\lambda_{\rm R}$ and $\lambda_{\rm KM}$ are the Rashba and Kane-Mele spin-orbit coupling paameters. [$\lambda_{\rm R} = 10\,$meV]

for the spin current operator $j_y^z = \hbar/4\,\{v_y, s_z\}$, where $\boldsymbol{v}$ corresponds to the velocity operator.

Our results for the spin Hall conductivity $\sigma_{\rm SHE}$ are shown in Fig. 3, with and without Kane-Mele SOC in the main panel and inset, respectively. For the pure Rashba system our real-space simulations capture the disorder-induced suppression of the intrinsic SHE, as shown in the inset of Fig. 3, in accordance with theoretical predictions based on covariant conservation laws and diagrammatic analysis of higher order scattering events [41]. Such result showcases the power of our methodology for the treatment of disorder effects. When including Kane-Mele SOC, our results show that outside the RPG the SHE remains similar to that of the pure Rashba system, while a prominent $\sigma_{\rm SHE}$ peak emerges from the band touching at charge neutrality. The inter-band transition originating this peak occurs between Dirac cones of opposite spin-pseudospin winding χ, which we find is proportional to the difference in entanglement between both Dirac cones (see Supplementary Note S1.). The $\sigma_{\rm SHE}$ peak is highly robust to disorder, as shown in Fig. 3; while, similar to the pure Rashba system, away from the charge neutrality point the SHE is suppressed. By these means, the interplay between Rashba and Kane-Mele SOC reinstates a finite SHE in a Rashba-Dirac system, even in the Rashba dominated regime where there is no topological quantum spin Hall effect gap. This result resembles that obtained for valley-Zeeman SOC, where the interplay with the Rashba field yields a finite SHE [41]. However, we note that in the latter case intervalley scattering strongly suppresses the SHE [32], while in the present system both intra and intervalley scattering act on the same level.

Altogether, our results unveil the role of spin-pseudospin correlations for spin-charge interconversion mechanisms in graphene. In particular, we have shown that spin-pseudospin entanglement can serve as a robust tool both to optimise spin-momentum locking in order to enhance the Rashba-Edelstein effect up to maximal efficiency; as well as to tune inter-band transitions generating a finite spin Hall effect. While we have here provided a proof of concept from a minimal graphene model, further research along this path may address these phenomena in other Dirac materials, as well as discern the effects of spin-pseudospin correlations for spin-orbit torque in magnetic devices.

METHODS

Quantum transport: framework

Under a driving electric field, the macroscopic non-equilibrium density of some observable $\mathcal{O}$, is given by Eq. (4), replacing the spin operator $\frac{\hbar}{2}s_y$ for $\mathcal{O}$. This expression may be further separated in Fermi surface and Fermi sea contributions [47]

$$\mathcal{O}_{\rm surf}(\varepsilon_{\rm F}) = \frac{\hbar}{\pi\Omega}\int {\rm d}\varepsilon\Big(-\frac{\partial f}{\partial\varepsilon}\Big)\,{\rm Tr}\left[{\rm Im}\,G^+\,\mathcal{O}\,{\rm Im}\,G^+\,(\boldsymbol{\mathcal{E}}\cdot\boldsymbol{j})\right], \tag{7a}$$

$$\mathcal{O}_{\rm sea}(\varepsilon_{\rm F}) = \frac{2\hbar}{\pi\Omega}\int {\rm d}\varepsilon f\;{\rm Im\,Tr}\left[{\rm Im}\,G^+\,\mathcal{O}\,\frac{\partial\,{\rm Re}\,G^+}{\partial\varepsilon}\,(\boldsymbol{\mathcal{E}}\cdot\boldsymbol{j})\right]. \tag{7b}$$

In the constant broadening approximation the system is considered to be periodic, while a finite yet small broadening $\eta > 0$ is introduced in the Green's function. The trace is taken in reciprocal space as $\Omega^{-1}\,{\rm Tr} \to \sum_n \int {\rm d}^2\boldsymbol{k}/(2\pi)^2$, where the sum is performed over all eigenstates. For the Fermi surface contribution we use $\sum_{n,m} {\rm Im}\,G^+(E_n)\,{\rm Im}\,G^+(E_m) = \sum_n ({\rm Im}\,G^+(E_n))^2$, and $\int {\rm d}\varepsilon\,\eta^2/(\varepsilon^2+\eta^2)^{-2} = \pi/2\eta$ to obtain

$$\mathcal{O}_{\rm surf}(\varepsilon_{\rm F}) = \tau_\eta \sum_n \int \frac{{\rm d}^2\boldsymbol{k}}{(2\pi)^2}\delta(E_{n,\boldsymbol{k}}-\varepsilon_{\rm F})\langle\mathcal{O}\rangle_{n,\boldsymbol{k}}\langle\boldsymbol{\mathcal{E}}\cdot\boldsymbol{j}\rangle_{n,\boldsymbol{k}}\,, \tag{8}$$

with $\tau_\eta = \hbar/2\eta$ the η-induced relaxation time. The Fermi sea contribution on the other hand is finite in the $\eta \to 0^+$ limit, given by

$$\mathcal{O}_{\rm sea}(\varepsilon_{\rm F}) = 2\hbar\sum_{n,m}\int \frac{{\rm d}^2\boldsymbol{k}}{(2\pi)^2} f(E_n)\,\frac{{\rm Im}\,\langle E_{n,\boldsymbol{k}}|\mathcal{O}|E_{m,\boldsymbol{k}}\rangle\langle E_{m,\boldsymbol{k}}|\boldsymbol{\mathcal{E}}\cdot\boldsymbol{j}|E_{n,\boldsymbol{k}}\rangle}{(E_{n,\boldsymbol{k}}-E_{m,\boldsymbol{k}})^2+\eta^2}\,. \tag{9}$$

The REE spin density and longitudinal current obtained in Eq. (5) are respectively calculated from Eq. (8) by replacing $\mathcal{O} \to \frac{\hbar}{2}s_y$ and $\mathcal{O} \to j_x = -ev_{\rm gr}\sigma_x$, where we have assumed $\boldsymbol{\mathcal{E}} = \mathcal{E}\hat{\boldsymbol{x}}$ exploiting the rotational symmetry of the system. The intrinsic spin Hall current, on the other hand, is a Fermi sea phenomena, obtained by replacing $\mathcal{O} \to j_y^z = \hbar/4\{v_y, s_z\}$ in Eq. (9).

Quantum transport: numerics

The raw output of our simulations is non-equilibrium expectation values of the form $\mathcal{O}_{\rm surf}$ and $\mathcal{O}_{\rm sea}$, as presented previously. Within the constant broadening approximation we use Eqs. (8) and (9), with the Bloch representation of the $\mathcal{O}$ and $\boldsymbol{j}$ operators and the bands derived from the Bloch Hamiltonian in Eq. (1), selecting an η value much smaller than all other energy scales of the system.

For real-space calculations in disordered systems we use Eqs. (7a) and (7b), along with real-space tight binding representations of the involved operators. The tight-binding graphene Hamiltonian is

$$\begin{aligned} H = &\sum_{\langle i,j\rangle} -\gamma_0 c_i^\dagger c_j + \frac{\mathrm{i}\lambda_{\rm R}}{3} c_i^\dagger \boldsymbol{s}\cdot\Big(\hat{\boldsymbol{z}}\times\frac{\boldsymbol{r}_{i,j}}{a_{\text{C-C}}}\Big)c_j + \\ &\sum_{\langle\langle i,j\rangle\rangle} \frac{\mathrm{i}\lambda_{\rm KM}}{6\sqrt{3}} c_i^\dagger s_z c_j\,\alpha_i \cos\Big(3\arccos\frac{\boldsymbol{r}_{\rm A\to B}\cdot\boldsymbol{r}_{i,j}}{\sqrt{3}a_{\text{C-C}}^2}\Big) + \\ &\sum_i w_i c_i^\dagger c_i \ , \end{aligned} \tag{10}$$

where $c_i^\dagger$ is the electron spinor creation operator at position $\boldsymbol{r}_i$, $\boldsymbol{r}_{i,j} = \boldsymbol{r}_i - \boldsymbol{r}_j$, and $\boldsymbol{r}_{\rm A\to B}$ is a vector pointing from a site of sublattice A to its nearest neighbour of sublattice B, with $a_{\text{C-C}} = 0.142\,\text{nm}$ the nearest neighbour distance, and $\alpha_i = \pm$ for $c_i^\dagger$ of sublattice A(B). Here $\gamma_0 = 2.7\,\text{eV}$ is the nearest neighbour hopping, $\lambda_{\rm R}$ and $\lambda_{\rm KM}$ are the Rashba and Kane-Mele SOC parameters respectively, and w_i is a random number from the uniform distribution $[-W/2, W/2]$ with W the Anderson disorder parameter.

Transport calculations are performed using the full Kubo-Bastin equation, given by Eqs. (7a) and (7b), solved by the kernel polynomial method (KPM) [48, 56]. The Green's function is expanded in Chebyshev polynomials using the Jackson kernel to damp the Gibbs oscillations, where the $\eta \to 0^+$ limit is taken; however, a spectral broadening is generated by the expansion. The resulting broadening parameter is $\eta_{\rm KPM} \approx \pi\Delta E/M$ at the band centre, with ΔE the bandwidth and M the order of the Chebyshev expansion [48]. To compute transport properties in the meV scale near the Dirac point we use an energy filtering technique allowing us to reach $\eta_{\rm KPM} \sim 1\,\text{meV}$ with $M = 800$, with a system size as large as 10^9 atoms [40]. Similar to the clean limit, the quasi-particle lifetime is given by $\tau_\eta(\varepsilon_{\rm F}) = \lim_{\eta\to 0^+}\frac{\hbar}{\pi}\int \mathrm{d}\varepsilon\,\eta^2/((\varepsilon_{\rm F}-\varepsilon)^2+\eta^2)^2$, where the Lorentzian function must be expanded in Chebyshev polynomials. We obtain

$$\begin{aligned} \tau_\eta(\varepsilon_{\rm F}) = &\frac{\hbar}{\pi\Delta E}\Bigg(\sum_{m_1,m_2\ \text{even}} + \sum_{m_1,m_2\ \text{odd}}\Bigg) g_{m_1}g_{m_2} \\ &T_{m_1}(\tilde{\varepsilon}_{\rm F})T_{m_2}(\tilde{\varepsilon}_{\rm F})\frac{(2-\delta_{0,m_1})(2-\delta_{0,m_2})}{1-\tilde{\varepsilon}_{\rm F}^2} \\ &\left(\frac{1}{1-(m_1+m_2)^2}+\frac{1}{1-(m_1-m_2)^2}\right) \\ \approx &\, 1.84\frac{\hbar}{2\eta(\varepsilon_{\rm F})}\ , \end{aligned} \tag{11}$$

with g_m the Jackson kernel coefficients, T_m the Chebyshev polynomials and $\tilde{\varepsilon}_{\rm F}$ the normalised $\varepsilon_{\rm F}$ within the values $[-1,1]$ by the bandwidth, and where the second equality was obtained by numerical calculation.

Our simulations also compute the spectral expectation value of some observable $\mathcal{O}$ in equilibrium, given by

$$\mathcal{O}(\varepsilon_{\rm F}) = -\frac{1}{\pi\Omega}\,\mathrm{Tr}\big[\mathrm{Im}G^+\,\mathcal{O}\big]\ , \tag{12}$$

which in the constant broadening approximation yields

$$\mathcal{O}(\varepsilon_{\rm F}) = -\frac{\eta}{\pi}\sum_n\int\frac{\mathrm{d}^2\boldsymbol{k}}{(2\pi)^2}\frac{\langle E_{n,\boldsymbol{k}}|\mathcal{O}|E_{n,\boldsymbol{k}}\rangle}{(E_{n,\boldsymbol{k}}-\varepsilon_{\rm F})^2+\eta^2}\ . \tag{13}$$

This is the case for the density of states, required to compute the REE efficiency, where we take $\mathcal{O}$ as the identity.

Transport velocity

In order to compute the REE efficiency in real-space disordered systems, we must construct a definition of the transport velocity which does not remount to band structure properties, but rather relies on macroscopic quantities which can be computed by the KPM simulations. Let's begin from the constant broadening approximation. The conductivity is given by Eq. (5b) of the main text, while the density of states is $\rho(\varepsilon_{\rm F}) = (\pi\Omega)^{-1}\mathrm{Tr}\,\mathrm{Im}\,G^+(\varepsilon_{\rm F}) = (2\pi)^{-1}\sum_{k_{\rm F}} k(\hbar v_{\rm gr}\langle\sigma_k\rangle)^{-1}$. The band structure Fermi velocity $v_{\rm F} = \hbar^{-1}\partial E/\partial k = v_{\rm gr}\langle\sigma_k\rangle$ can thus be obtained as $v(\varepsilon_{\rm F}) = \sqrt{2\sigma(\varepsilon_{\rm F})/e^2\rho(\varepsilon_{\rm F})\tau_\eta(\varepsilon_{\rm F})}$ within the RPG. We now offer an interpretation of this quantity in terms of the carrier wave packet evolution. We may use the Einstein relation to write the conductivity as $\sigma(\varepsilon_{\rm F}) = e^2\rho(\varepsilon_{\rm F})D$, with $D(\varepsilon_{\rm F}) = \lim_{t\to\infty}\Delta X^2(\varepsilon_{\rm F},t)/2t$ the diffusion coefficient, where $\Delta X^2(\varepsilon_{\rm F},t)$ is the mean square displacement of the wave packet, and t its evolution time. The largest time scale accessible within the KPM simulations corresponds to τ_η, which can be interpreted as the carrier quasi-particle coherence time [49]. We thus take $D(\varepsilon_{\rm F}) = \Delta X^2(\varepsilon_{\rm F},\tau_\eta)/2\tau_\eta$. With this, the transport velocity reads $v(\varepsilon_{\rm F}) = \sqrt{\Delta X^2(\varepsilon_{\rm F},\tau_\eta)}/\tau_\eta$, which we interpret as the mean velocity of the carriers throughout their evolution.

CODE AVAILABILITY

The computer codes used to produce the numerical results are available from the corresponding authors upon request.

DATA AVAILABILITY

The data that support the findings of this study are available from the corresponding authors upon request.

* Corresponding Author joaquin.medina@icn2.cat
† Corresponding Author josehugo.garcia@icn2.cat

REFERENCES

[1] J. Sinova, S. O. Valenzuela, J. Wunderlich, C. Back, and T. Jungwirth, Spin hall effects, Reviews of Modern Physics **87**, 1213–1260 (2015).
[2] A. Manchon, H. C. Koo, J. Nitta, S. M. Frolov, and R. A. Duine, New perspectives for Rashba spin–orbit coupling, Nature Materials **14**, 871 (2015).
[3] J. F. Sierra, J. Fabian, R. K. Kawakami, S. Roche, and S. O. Valenzuela, Van der Waals heterostructures for spintronics and opto-spintronics, Nature Nanotechnology **16**, 856 (2021).
[4] H. Yang, S. O. Valenzuela, M. Chshiev, S. Couet, B. Dieny, B. Dlubak, A. Fert, K. Garello, M. Jamet, D.-E. Jeong, K. Lee, T. Lee, M.-B. Martin, G. S. Kar, P. Sénéor, H.-J. Shin, and S. Roche, Two-dimensional materials prospects for non-volatile spintronic memories, Nature **606**, 663 (2022).
[5] S. Roche, B. van Wees, K. Garello, and S. O. Valenzuela, Spintronics with two-dimensional materials and van der waals heterostructures, 2D Materials **11**, 043001 (2024).
[6] E. C. Ahn, 2d materials for spintronic devices, npj 2D Materials and Applications **4**, 10.1038/s41699-020-0152-0 (2020).
[7] Z. Zhao, Y. Lin, and A. Avsar, Novel spintronic effects in two-dimensional van der waals heterostructures, npj 2D Materials and Applications **9**, 10.1038/s41699-025-00546-4 (2025).
[8] N. Tombros, C. Jozsa, M. Popinciuc, H. T. Jonkman, and B. J. van Wees, Electronic spin transport and spin precession in single graphene layers at room temperature, Nature **448**, 571–574 (2007).
[9] P. J. Zomer, M. H. D. Guimarães, N. Tombros, and B. J. van Wees, Long-distance spin transport in high-mobility graphene on hexagonal boron nitride, Physical Review B **86**, 10.1103/physrevb.86.161416 (2012).
[10] H. Wen, H. Dery, W. Amamou, T. Zhu, Z. Lin, J. Shi, I. Žutić, I. Krivorotov, L. Sham, and R. K. Kawakami, Experimental demonstration of xor operation in graphene magnetologic gates at room temperature, Physical Review Applied **5**, 10.1103/physrevapplied.5.044003 (2016).
[11] D. Khokhriakov, S. Sayed, A. M. Hoque, B. Karpiak, B. Zhao, S. Datta, and S. P. Dash, Multifunctional spin logic operations in graphene spin circuits, Physical Review Applied **18**, 10.1103/physrevapplied.18.064063 (2022).
[12] Z. Wang, D.-K. Ki, H. Chen, H. Berger, A. H. MacDonald, and A. F. Morpurgo, Strong interface-induced spin–orbit interaction in graphene on WS_2, Nature Commun. **6**, 8339 (2015).
[13] Z. Wang, D.-K. Ki, J. Y. Khoo, D. Mauro, H. Berger, L. S. Levitov, and A. F. Morpurgo, Origin and magnitude of 'designer' spin-orbit interaction in graphene on semiconducting transition metal dichalcogenides, Phys. Rev. X **6**, 041020 (2016).
[14] L. Sun, L. Rademaker, D. Mauro, A. Scarfato, A. Pásztor, I. Gutiérrez-Lezama, Z. Wang, J. Martinez-Castro, A. F. Morpurgo, and C. Renner, Determining spin-orbit coupling in graphene by quasiparticle interference imaging, Nature Communications **14**, 10.1038/s41467-023-39453-x (2023).
[15] Q. Rao, W.-H. Kang, H. Xue, Z. Ye, X. Feng, K. Watanabe, T. Taniguchi, N. Wang, M.-H. Liu, and D.-K. Ki, Ballistic transport spectroscopy of spin-orbit-coupled bands in monolayer graphene on WSe2, Nature Communications **14**, 10.1038/s41467-023-41826-1 (2023).
[16] A. M. Hoque, D. Khokhriakov, K. Zollner, B. Zhao, B. Karpiak, J. Fabian, and S. P. Dash, All-electrical creation and control of spin-galvanic signal in graphene and molybdenum ditelluride heterostructures at room temperature, Commun. Phys. **4**, 10.1038/s42005-021-00611-6 (2021).
[17] P. Tiwari, M. K. Jat, A. Udupa, D. S. Narang, K. Watanabe, T. Taniguchi, D. Sen, and A. Bid, Experimental observation of spin-split energy dispersion in high-mobility single-layer graphene/WSe2 heterostructures, npj 2D Materials and Applications **6**, 10.1038/s41699-022-00348-y (2022).
[18] J. F. Sierra, J. Světlík, W. Savero Torres, L. Camosi, F. Herling, T. Guillet, K. Xu, J. S. Reparaz, V. Marinova, D. Dimitrov, and S. O. Valenzuela, Room-temperature anisotropic in-plane spin dynamics in graphene induced by pdse2 proximity, Nature Materials **24**, 876–882 (2025).
[19] D. Khokhriakov, A. W. Cummings, K. Song, M. Vila, B. Karpiak, A. Dankert, S. Roche, and S. P. Dash, Tailoring emergent spin phenomena in dirac material heterostructures, Science Advances **4**, 10.1126/sciadv.aat9349 (2018).
[20] P. Lee, K.-H. Jin, S. J. Sung, J. G. Kim, M.-T. Ryu, H.-M. Park, S.-H. Jhi, N. Kim, Y. Kim, S. U. Yu, K. S. Kim, D. Y. Noh, and J. Chung, Proximity effect induced electronic properties of graphene on Bi2Te2Se, ACS Nano **9**, 10861–10866 (2015).
[21] K. Song, D. Soriano, A. W. Cummings, R. Robles, P. Ordejón, and S. Roche, Spin proximity effects in graphene/topological insulator heterostructures, Nano Letters **18**, 2033–2039 (2018).
[22] T. Naimer and J. Fabian, Twist-angle dependent proximity induced spin-orbit coupling in graphene/topological insulator heterostructures, Physical Review B **107**, 195144 (2023).
[23] C. K. Safeer, J. Ingla-Aynés, F. Herling, J. H. Garcia, M. Vila, N. Ontoso, M. R. Calvo, S. Roche, L. E. Hueso, and F. Casanova, Room-temperature spin hall ef-

fect in graphene/mos2 van der waals heterostructures, Nano Letters **19**, 1074–1082 (2019).

[24] T. S. Ghiasi, A. A. Kaverzin, P. J. Blah, and B. J. van Wees, Charge-to-spin conversion by the rashba–edelstein effect in two-dimensional van der waals heterostructures up to room temperature, Nano Letters **19**, 5959–5966 (2019).

[25] L. A. Benítez, W. S. Torres, J. F. Sierra, M. Timmermans, J. H. García, S. Roche, M. V. Costache, and S. O. Valenzuela, Tunable room-temperature spin galvanic and spin Hall effects in van der Waals heterostructures, Nature Mater **19**, 170 (2020).

[26] D. Khokhriakov, A. M. Hoque, B. Karpiak, and S. P. Dash, Gate-tunable spin-galvanic effect in graphene-topological insulator van der waals heterostructures at room temperature, Nature Communications **11**, 10.1038/s41467-020-17481-1 (2020).

[27] M. I. Katsnelson, K. S. Novoselov, and A. K. Geim, Chiral tunnelling and the klein paradox in graphene, Nature Physics **2**, 620–625 (2006).

[28] A. F. Morpurgo and F. Guinea, Intervalley scattering, long-range disorder, and effective time-reversal symmetry breaking in graphene, Physical Review Letters **97**, 10.1103/physrevlett.97.196804 (2006).

[29] E. McCann, K. Kechedzhi, V. I. Fal'ko, H. Suzuura, T. Ando, and B. L. Altshuler, Weak-localization magnetoresistance and valley symmetry in graphene, Physical Review Letters **97**, 10.1103/physrevlett.97.146805 (2006).

[30] K. S. Novoselov, A. K. Geim, S. V. Morozov, D. Jiang, M. I. Katsnelson, I. V. Grigorieva, S. V. Dubonos, and A. A. Firsov, Two-dimensional gas of massless dirac fermions in graphene, Nature **438**, 197–200 (2005).

[31] Y. Zhang, Y.-W. Tan, H. L. Stormer, and P. Kim, Experimental observation of the quantum hall effect and berry's phase in graphene, Nature **438**, 201–204 (2005).

[32] J. H. Garcia, A. W. Cummings, and S. Roche, Spin hall effect and weak antilocalization in graphene/transition metal dichalcogenide heterostructures, Nano Letters **17**, 5078–5083 (2017).

[33] F. Sousa, D. T. S. Perkins, and A. Ferreira, Weak localisation driven by pseudospin-spin entanglement, Communications Physics **5**, 10.1038/s42005-022-01066-z (2022).

[34] D. V. Tuan, F. Ortmann, D. Soriano, S. O. Valenzuela, and S. Roche, Pseudospin-driven spin relaxation mechanism in graphene, Nature Phys. **10**, 857 (2014).

[35] K. S. Denisov, I. V. Rozhansky, S. O. Valenzuela, and I. Žutić, Terahertz spin-light coupling in proximitized dirac materials, Physical Review B **109**, 10.1103/physrevb.109.l201406 (2024).

[36] A. Dyrdał, J. Barnaś, and V. K. Dugaev, Current-induced spin polarization in graphene due to rashba spin-orbit interaction, Physical Review B **89**, 10.1103/physrevb.89.075422 (2014).

[37] M. Offidani, M. Milletarì, R. Raimondi, and A. Ferreira, Optimal charge-to-spin conversion in graphene on transition-metal dichalcogenides, Phys. Rev. Lett. **119**, 196801 (2017).

[38] B. G. de Moraes, A. W. Cummings, and S. Roche, Emergence of intraparticle entanglement and time-varying violation of Bell's inequality in Dirac matter, Phys. Rev. B **102**, 041403(R) (2020).

[39] F. Sousa, G. Tatara, and A. Ferreira, Skew-scattering-induced giant antidamping spin-orbit torques: Collinear and out-of-plane Edelstein effects at two-dimensional material/ferromagnet interfaces, Phys. Rev. Res. **2**, 043401 (2020).

[40] J. Medina Dueñas, J. H. García, and S. Roche, Emerging spin-orbit torques in low-dimensional Dirac materials, Phys. Rev. Lett. **132**, 266301 (2024).

[41] M. Milletarì, M. Offidani, A. Ferreira, and R. Raimondi, Covariant conservation laws and the spin hall effect in dirac-rashba systems, Phys. Rev. Lett. **119**, 246801 (2017).

[42] X. Wang, J. Tang, X. Xia, C. He, J. Zhang, Y. Liu, C. Wan, C. Fang, C. Guo, W. Yang, Y. Guang, X. Zhang, H. Xu, J. Wei, M. Liao, X. Lu, J. Feng, X. Li, Y. Peng, H. Wei, R. Yang, D. Shi, X. Zhang, Z. Han, Z. Zhang, G. Zhang, G. Yu, and X. Han, Current-driven magnetization switching in a van der waals ferromagnet fe3gete2, Science Advances **5**, 10.1126/sciadv.aaw8904 (2019).

[43] C. Weeks, J. Hu, J. Alicea, M. Franz, and R. Wu, Engineering a robust quantum spin hall state in graphene via adatom deposition, Physical Review X **1**, 10.1103/physrevx.1.021001 (2011).

[44] A. Cresti, B. K. Nikolic, J. H. Garcia, and S. Roche, Charge, spin and valley hall effects in disordered graphene, La Rivista del Nuovo Cimento **39**, 587 (2016).

[45] K. Hatsuda, H. Mine, T. Nakamura, J. Li, R. Wu, S. Katsumoto, and J. Haruyama, Evidence for a quantum spin hall phase in graphene decorated with Bi2Te3 nanoparticles, Science Advances **4**, 10.1126/sciadv.aau6915 (2018).

[46] W. K. Wootters, Entanglement of formation of an arbitrary state of two qubits, Phys. Rev. Lett. **80**, 2245 (1998).

[47] V. Bonbien and A. Manchon, Symmetrized decomposition of the Kubo-Bastin formula, Phys. Rev. B **102**, 085113 (2020).

[48] A. Weisse, G. Wellein, A. Alvermann, and H. Fehske, The kernel polynomial method, Rev. Mod. Phys. **78**, 275 (2006).

[49] Z. Fan, J. H. García, A. W. Cummings, J. E. Barrios-Vargas, M. Panhans, A. Harju, F. Ortmann, and S. Roche, Linear scaling quantum transport methodologies, Physics Reports Linear scaling quantum transport methodologies, **903**, 1 (2021).

[50] S. G. de Castro, J. M. V. P. Lopes, A. Ferreira, and D. Bahamon, Fast fourier-chebyshev approach to real-space simulations of the kubo formula, Physical Review Letters **132**, 10.1103/physrevlett.132.076302 (2024).

[51] S. G. de Castro, A. Ferreira, and D. A. Bahamon, Efficient chebyshev polynomial approach to quantum conductance calculations: Application to twisted bilayer graphene, Physical Review B **107**, 10.1103/physrevb.107.045418 (2023).

[52] C. L. Kane and E. J. Mele, Quantum spin hall effect in graphene, Physical Review Letters **95**, 10.1103/physrevlett.95.226801 (2005).

[53] L. Sheng, D. N. Sheng, C. S. Ting, and F. D. M. Haldane, Nondissipative spin hall effect via quantized edge transport, Physical Review Letters **95**, 10.1103/physrevlett.95.136602 (2005).

[54] J. M. da Silva, F. A. F. Santana, J. G. G. S. Ramos, and A. L. R. Barbosa, Spin hall angle in single-layer graphene, Journal of Applied Physics **132**, 10.1063/5.0107212 (2022).

[55] A. Dyrdał, V. K. Dugaev, and J. Barnaś, Spin hall effect in a system of dirac fermions in the honeycomb lattice

with intrinsic and rashba spin-orbit interaction, Physical Review B **80**, 10.1103/physrevb.80.155444 (2009).
[56] J. H. García, L. Covaci, and T. G. Rappoport, Real-space calculation of the conductivity tensor for disordered topological matter, Phys. Rev. Lett. **114**, 116602 (2015).

ACKNOWLEDGMENTS

We thank Aires Ferreira for fruitful discussions on the state of the art of SCI. The authors acknowledge funding from: grant PID2022-138283NB-I00 funded by MICIU/AEI/10.13039/501100011033 and by "ERDF/EU"; ERC project AI4SPIN funded by Horizon Europe-European Research Council Executive Agency under grant agreement No 101078370-AI4SPIN. J.M.D. acknowledges support from MICIU grant FPI PRE2021-097031. ICN2 is funded by the CERCA Programme/Generalitat de Catalunya and supported by the Severo Ochoa Centres of Excellence programme, Grant CEX2021-001214-S, funded by MCIN/AEI/10.13039.501100011033.

AUTHOR CONTRIBUTIONS

J. M. D. designed the research, obtained main theoretical results, and wrote the manuscript. S. G. de C. developed and ran the computer code to obtain numerical results. J. H. G. and S. R. co-supervised the project.

COMPETING INTERESTS

The authors declare no competing interests.